Journal of Computational Physics **156,** 300–324 (1999)
Article ID jcph.1999.6363, available online at http://www.idealibrary.com on IDEAL®

Different Modes of Rayleigh–Bénard Instability in Two- and Three-Dimensional Rectangular Enclosures

Alexander Yu. Gelfgat

Computational Mechanics Laboratory, Faculty of Mechanical Engineering, Technion—Israel Institute of Technology, Haifa 32000, Israel

Received February 16, 1999; revised June 28, 1999

The article describes a complete numerical solution of a recently formulated benchmark problem devoted to the parametric study of Rayleigh–Bénard instability in rectangular two- and three-dimensional boxes. The solution is carried out by the spectral Galerkin method with globally defined, three-dimensional, divergent-free basis functions, which satisfy all boundary conditions. The general description of these three-dimensional basis functions, which can be used for a rather wide spectrum of problems, is presented. The results of the parametric calculations are presented as neutral curves showing the dependence of the critical Rayleigh number on the aspect ratio of the cavity. The neutral curves consist of several continuous branches, which belong to different modes of the most dangerous perturbation. The patterns of different perturbations are also reported. The results obtained lead to some new conclusions about the patterns of the most dangerous perturbations and about the similarities between two- and three-dimensional models. Some extensions of the considered benchmark problem are discussed.

Key Words: global Galerkin method; finite volume method; Rayleigh–Bénard instability.

1. INTRODUCTION

The study of the stability and multiplicity of numerical solutions leads to an eigenvalue problem whose order is usually so large that a numerical solution becomes extremely difficult. Although the corresponding numerical codes and new numerical approaches are being extensively developed recently, there is a considerable lack of theoretical and numerical results, which can be used for comparison and validation of numerical codes. This paper is devoted to a relatively simple benchmark problem recently formulated for the validation of CFD methods containing stability analysis and path-continuation techniques.

0021-9991/99 $30.00

The benchmark problem was proposed at EUROMECH/EUROFTAC Colloquium 383 on Continuation Methods in Fluid Dynamics [1].

The study of the stability of calculated fluid flows (assuming that the basic state is unknown and has to be calculated) usually is carried out by time-forward integration of the corresponding equations. This leads to CPU-time consuming computations and does not allow one to perform a detailed parametric study. Direct studies of stability and multiplicity, which involve calculation of the Jacobian matrices, their determinants, and eigenvalues, became possible only recently. A description of the main approaches, which involve the calculation of leading eigenvalues of the sparse Jacobian matrix by different versions of the Arnoldi method, can be found in [2, 3] and references therein. Another approach was proposed in [4] and was successfully used for parametric stability studies in [5–8]. The latter approach uses the global spectral method to reduce the number of degrees of freedom of the numerical model and to calculate the spectrum of Jacobian matrices of much smaller size.

The best known CFD benchmark problem, which considers the instability of steady flows, was formulated in [9]. However, most of the calculations reported in [9], as well as those performed later, were done by a straightforward numerical integration in time. To the best of our knowledge, the linear stability analysis of this problem was performed numerically only in [4, 10]. Apparently, this benchmark remains too difficult for numerical stability calculations, and another simpler benchmark problem can attract a wider attention. Such a problem was formulated recently in [1]. This benchmark problem is devoted to the Rayleigh–Bénard instability in confined rectangular two- and three-dimensional containers. The problem is less difficult than others (e.g., [9]) because (i) the basic state (non-uniformly heated quiescent fluid) is known and simple and (ii) the spectrum of the linear stability problem is purely real (i.e., only steady bifurcation is possible). This allows one to validate parts of numerical codes devoted to stability analysis without preliminary calculation of the basic state. The existence of two- and three-dimensional subproblems also is an important advantage.

The present paper describes a complete solution of the benchmark problem by the global Galerkin method. The two-dimensional version of the approach is described in [4] and was used for the study of stability of two-dimensional convective flows in [7, 8]. The three-dimensional version of this numerical approach is described here for the first time.

The physics of the Rayleigh–Bénard instability is well understood [11–13]. A review of the enormous amount of experimental, theoretical, and numerical studies devoted to this phenomena can be found in [13]. Most of these studies considered infinite fluid layers. Consideration of this phenomenon in closed two-dimensional cavities also does not cause numerical difficulties [14–17]. However, as it is shown here, the detailed parametric study for three-dimensional rectangular containers leads to several new conclusions. Thus, as it was shown for the Bénard–Marangoni instability [18], the possible multiplicity of supercritical states and possible similarities between two- and three-dimensional results become clearer.

The article is organized as follows. Section 2 contains the formulation of the problem and description of some known theoretical results. The numerical method is described in Section 3. Section 4 contains a series of test calculations, which are essential for the validation of further results. Results for two- and three-dimensional benchmark subproblems are described in Sections 5 and 6, respectively. The conclusions are drawn in Section 7.

2. FORMULATION OF THE PROBLEM

2.1. *The Full Problem*

Convection of a Boussinesq fluid in a rectangular two- or three-dimensional rectangular cavity is considered. The flow is described by the dimensionless Boussinesq equations

$$Pr^{-1}\left[\frac{\partial \mathbf{v}}{\partial t} + (\mathbf{v}\cdot\nabla)\mathbf{v}\right] = -\nabla p + \Delta \mathbf{v} + Ra\,\theta \mathbf{e}_z \tag{1}$$

$$\nabla \cdot \mathbf{v} = 0 \tag{2}$$

$$\frac{\partial \theta}{\partial t} + (\mathbf{v}\cdot\nabla)\theta = \Delta\theta, \tag{3}$$

where $\mathbf{v} = (v_x, v_y, v_z)$ is the fluid velocity, $\theta = (\bar{\theta} - \bar{\theta}_A)/(\bar{\theta}_B - \bar{\theta}_A)$ the temperature, p the pressure, $\bar{\theta}_A$ and $\bar{\theta}_B$ are the temperatures of the ambient and the bottom, respectively, $Ra = \overline{g\alpha}(\bar{\theta}_B - \bar{\theta}_A)\bar{d}^3/\overline{\nu\kappa}$ the Rayleigh number, $Pr = \bar{\nu}/\bar{\chi}$ the Prandtl number, $\bar{g}$ the gravity acceleration, $\bar{\alpha}$ the thermal expansion coefficient, $(\bar{\theta}_B - \bar{\theta}_A)$ the characteristic temperature difference, $\bar{\nu}$ the kinematic viscosity, $\bar{\kappa}$ the thermal diffusivity, $\bar{d}$ the height of the cavity, and $\mathbf{e}_z$ is the unit vector in the z-direction (the overbar indicates dimensional variables).

It is assumed that the lower and the lateral boundaries are no-slip, the upper boundary is stress-free, the lower boundary is isothermal, the lateral boundaries are thermally insulated, and a convective cooling condition characterized by a Biot number Bi is imposed on the upper boundary. The dimensionless boundary conditions are

$$z = 0 \qquad \theta = 1, \qquad \mathbf{v} = 0 \tag{4}$$

$$z = 1 \qquad \frac{\partial \theta}{\partial z} = -Bi\,\theta, \qquad v_z = \frac{\partial v_x}{\partial z} = \frac{\partial v_y}{\partial z} = 0 \tag{5}$$

$$x = 0, A_x \qquad \frac{\partial \theta}{\partial x} = 0, \qquad \mathbf{v} = 0 \tag{6}$$

$$y = 0, A_y \qquad \frac{\partial \theta}{\partial y} = 0, \qquad \mathbf{v} = 0. \tag{7}$$

Here $A_x = \bar{L}_x/\bar{d}$, $A_y = \bar{L}_y/\bar{d}$ are the aspect ratios of the cavity in the x- and y-directions, respectively. The solution of the problem (1)–(7), corresponding to the quiescent state, is

$$\mathbf{v}_0 = 0, \qquad p_0 = Ra\left(z - \frac{1}{2}\frac{Bi}{1+Bi}z^2\right), \qquad \theta_0 = 1 - \frac{Bi}{1+Bi}z. \tag{8}$$

The benchmark problem [1] requires us to calculate the critical values Ra_{cr} of the Rayleigh number, corresponding to bifurcation from the quiescent state to convective motion, for the following cases:

- Two-dimensional problems ($A_y = \infty$):
  Problem 1. Compute Ra_{cr} as a function of $A_x \in [1, 10]$ for fixed $Bi = 1$;
  Problem 2. Compute Ra_{cr} as a function of $Bi \in [1, 10]$ for fixed $A_x = 10$;
  Problem 3. Compute the pattern of the critical mode for the case $A_x = 10$, $Bi = 1$.
- Three-dimensional problems:
  Problem 4. Compute Ra_{cr} as a function of $A_x = A_y \in [1, 8]$ for fixed $Bi = 1$;
  Problem 5. Compute the patterns of the critical modes for the case $A_y = 4$, $Bi = 1$ for several values of $A_x \in [1, 8]$.

2.2. *Linear Stability Problem and Some Theoretical Considerations*

Following the linear stability theory [11,12], we introduce perturbations $\mathbf{v}'$, p', and θ' of the initial state $(\mathbf{v}_0, \theta_0)$ as

$$\mathbf{v} = \mathbf{v}_0 + \varepsilon\mathbf{v}', \qquad p = p_0 + \varepsilon p', \qquad \theta = \theta_0 + \varepsilon\theta', \tag{9}$$

where ε is a perturbation amplitude which is assumed to be infinitely small. After substitution of (9) in Eqs. (1)–(3) and neglecting all terms of order higher than ε, the problem for perturbations becomes

$$Pr^{-1}\frac{\partial \mathbf{v}'}{\partial t} = -\nabla p' + \Delta\mathbf{v}' + Ra\,\theta'\mathbf{e}_z \tag{10}$$

$$\nabla\cdot\mathbf{v}' = 0 \tag{11}$$

$$\frac{\partial\theta'}{\partial t} - \frac{Bi}{1+Bi}v_z' = \Delta\theta'. \tag{12}$$

Following [11, 12] we represent the perturbations $\mathbf{v}'$, p', and θ' in the form

$$\{\mathbf{v}', p', \theta'\} = \{\mathbf{u}(x, y, z), P(x, y, z), \Theta(x, y, z)\}\exp(\lambda t), \tag{13}$$

where the new unknown functions $\mathbf{u} = (u_x, u_y, u_z)$, P, and Θ depend on the spatial coordinates only. Equations (10)–(12) become

$$\lambda Pr^{-1}\mathbf{u} = -\nabla P + \Delta\mathbf{u} + Ra\,\Theta\mathbf{e}_z \tag{14}$$

$$\nabla\cdot\mathbf{u} = 0 \tag{15}$$

$$\lambda\Theta - \frac{Bi}{1+Bi}u_z = \Delta\Theta. \tag{16}$$

The boundary conditions for $\mathbf{u}$, P, and Θ follow from (4)–(8),

$$z = 0 \qquad \Theta = 0, \qquad \mathbf{u} = 0 \tag{17}$$

$$z = 1 \qquad \frac{\partial\Theta}{\partial z} = -Bi\Theta, \qquad u_z = \frac{\partial u_x}{\partial z} = \frac{\partial u_y}{\partial z} = 0 \tag{18}$$

$$x = 0, A_x \qquad \frac{\partial\Theta}{\partial x} = 0, \qquad \mathbf{u} = 0 \tag{19}$$

$$y = 0, A_y \qquad \frac{\partial\Theta}{\partial y} = 0, \qquad \mathbf{u} = 0. \tag{20}$$

Equations (14)–(20) define the eigenproblem for the eigenvalues λ and the eigenfunctions $\mathbf{u}$, P, and Θ. The initial state $(\mathbf{v}_0, \theta_0)$ is unstable if there exists at least one eigenvalue λ, such that $\mathrm{Real}(\lambda) > 0$. Therefore, the solution of the stability problem requires us to determine the critical value of the Rayleigh number Ra_{cr}, for which the largest real part of all the eigenvalues is zero. In other words, the marginal stability condition is $\mathrm{Real}[\Lambda(Ra_{cr})] = 0$, where Λ is the dominant eigenvalue (the eigenvalue with the largest real part). The eigenfunctions corresponding to the dominant eigenvalue define the most critical mode of the stability problem.

It is well known that the spectrum of the Rayleigh–Bénard stability problem is real (see [11, 12], for example). Thus, the considered problem is simplified: it is necessary to look for $Ra_{cr} > 0$, for which the dominant eigenvalue Λ is the exact zero. Additionally, as it follows from (14), the values of the parameters Ra, A_x, and A_y for which $\lambda = 0$ do not depend on

the Prandtl number. Therefore in all calculations we consider $Pr = 1$ without any loss of generality.

3. NUMERICAL METHOD

We use the Galerkin method with globally defined basis functions, which satisfy all the boundary conditions and the continuity equation. The described numerical approach was proposed for the solution of hydrodynamic stability problems in [4]. It was successfully used for the analysis of stability of axisymmetric swirling [5, 6] and two-dimensional convective [7, 8] flows. Detailed data on several two-dimensional test problems, solved by this numerical approach, can be found in [4–8]. In the present paper we focus only on the three-dimensional set of the basis functions in Cartesian coordinates. The set of the basis functions for the two-dimensional formulation is a particular case of the three-dimensional case and was described in detail in [4].

The three-dimensional divergence-free velocity vector can be represented as (see also [18])

$$\mathbf{v} = \begin{pmatrix} v_x \\ v_y \\ v_z \end{pmatrix} = \begin{pmatrix} v_x \\ v_y \\ -\int \left(\frac{\partial v_x}{\partial x} + \frac{\partial v_y}{\partial y} \right) dz \end{pmatrix} = \begin{pmatrix} v_x \\ 0 \\ -\int \frac{\partial v_x}{\partial x}\, dz \end{pmatrix} + \begin{pmatrix} 0 \\ v_y \\ -\int \frac{\partial v_y}{\partial y}\, dz \end{pmatrix}. \quad (21)$$

The two terms on the right hand side of (21) can be interpreted as the projections of velocity on the xy- ($y = \text{const}$) and xz- ($x = \text{const}$) planes, respectively. Therefore, to represent the three-dimensional velocity vector as a Galerkin series, it is necessary to define two independent sets of basis functions which will allow us to approximate the projections of the velocity on these planes. The velocity is approximated as

$$\mathbf{v} \approx \sum_{i=0}^{N_x} \sum_{j=0}^{N_y} \sum_{k=0}^{N_z} \left[c_{ijk}^{(x)}(t) \mathbf{w}_{ijk}^{(x)}(x, y, z) + c_{ijk}^{(y)}(t) \mathbf{w}_{ijk}^{(y)}(x, y, z) \right], \quad (22)$$

where $c_{ijk}^{(x)}$ and $c_{ijk}^{(y)}$ are unknown time-dependent coefficients and $\mathbf{w}_{ijk}^{(x)}$ and $\mathbf{w}_{ijk}^{(y)}$ are the basis functions in the planes $x = \text{const}$ and $y = \text{const}$, respectively. These functions are defined as

$$\mathbf{w}_{ijk}^{(x)}(x, y, z) = \begin{Bmatrix} 0 \\ \sum_{m=0}^{4} \tilde{f}_{im} T_{i+m}\left(\frac{x}{A_x}\right) \sum_{l=0}^{4} \frac{\tilde{g}_{jl}}{2(j+1)} T_{j+l}\left(\frac{y}{A_y}\right) \sum_{n=0}^{4} \tilde{h}_{kn} U_{k+n-1}(z) \\ -\sum_{m=0}^{4} \tilde{f}_{im} T_{i+m}\left(\frac{x}{A_x}\right) \sum_{l=0}^{4} \tilde{g}_{jl} U_{j+l-1}\left(\frac{y}{A_y}\right) \sum_{n=0}^{4} \frac{\tilde{h}_{kn}}{2(k+n)} T_{k+n}(z) \end{Bmatrix}, \quad (23)$$

$$\mathbf{w}_{ijk}^{(y)}(x, y, z) = \begin{Bmatrix} \sum_{m=0}^{4} \frac{\hat{f}_{im}}{2(i+m)} T_{i+m}\left(\frac{x}{A_x}\right) \sum_{l=0}^{4} \hat{g}_{jl} T_{j+l}\left(\frac{y}{A_y}\right) \sum_{n=0}^{4} \hat{h}_{kn} U_{k+n-1}(z) \\ -\sum_{m=0}^{4} \hat{f}_{im} U_{i+m-1}\left(\frac{x}{A_x}\right) \sum_{l=0}^{4} \hat{g}_{jl} T_{j+l}\left(\frac{y}{A_y}\right) \sum_{n=0}^{4} \frac{\hat{h}_{kn}}{2(k+n)} T_{k+n}(z) \end{Bmatrix}, \quad (24)$$

where T_n and U_n are the Chebyshev polynomials of the first and the second type, respectively,

$$T_n(x) = \cos[n \arccos(2x-1)], \qquad U_n(x) = \frac{\sin[(n+1)\arccos(2x-1)]}{\sin[\arccos(2x-1)]}. \quad (25)$$

Because of the relation between the Chebyshev polynomials $(d/dx)T_{n+1}(x) = = 2(n+1)U_n(x)$ the basis functions (23), (24) are divergence-free and therefore the approximation of the velocity (22) is analytically divergence-free for any number of Galerkin modes. Substitution of (23), (24) in the boundary conditions (e.g., (17)–(20)) defines a set of linear equations for the coefficients $\tilde{f}_{im}$, $\hat{f}_{im}$, $\tilde{g}_{jl}$, $\hat{g}_{jl}$, $\tilde{h}_{im}$, $\hat{h}_{im}$. After these coefficients are determined, the Galerkin series (22) satisfy all the linear homogeneous boundary conditions analytically (for details see [4]). Note also that the projection of the pressure gradient on the divergent-free basis (23), (24) is analytically zero [4], which means that the Galerkin procedure eliminates the perturbation of pressure from (14). Therefore, we do not need an approximation of the pressure. A similar spectral approach was used in [18] for the study of the Bénard–Marangoni instability in three-dimensional boxes. However, the basis functions used there were restricted to the certain boundary conditions: most of the boundary conditions were satisfied analytically while several others (including the boundary condition with Biot number) were satisfied numerically. The present definition of the basis functions allows one to satisfy analytically (and without exceptions) an arbitrary set of linear boundary conditions.

The Galerkin series for the temperature is defined in a similar way,

$$\theta = \left(1 - \frac{Bi}{1+Bi}z\right) + \sum_{i=0}^{N_x}\sum_{j=0}^{N_y}\sum_{k=0}^{N_z} d_{ijk}(t)q_{ij}(x,y,z), \quad (26)$$

where

$$q_{ij}(x,y,z) = \sum_{m=0}^{2} p_{im}T_{i+m}\left(\frac{x}{A_x}\right)\sum_{l=0}^{2} q_{jl}T_{j+l}\left(\frac{y}{A_y}\right)\sum_{n=0}^{2} r_{jn}T_{j+n}(z) \quad (27)$$

and the coefficients p_{il}, q_{il}, and r_{il} are defined to satisfy all the temperature boundary conditions (17)–(20). Linear combinations of the Chebyshev polynomials, similar to (27), were used in [19] for solution of the one-dimensional Orr–Sommerfeld equation.

Application of the Galerkin method to the linear stability problem (14)–(20) leads to the algebraic eigenvalue problem (we consider $Pr = 1$, as it was mentioned above)

$$\sum_{J=1}^{N} \mathbf{L}_{IJ}\mathbf{X}_J = \lambda \mathbf{X}_I, \quad (28)$$

where the N-dimensional vector $\mathbf{X}$ consists of all the coefficients d_{ijk}, $c^{(x)}_{ijk}$, and $c^{(y)}_{ijk}$, $N = 3 \times N_x \times N_y \times N_z$ is the total number of the Galerkin modes (degrees of freedom), and the matrix $\mathbf{L}$ is composed from 9 matrices $\mathbf{D}_{xx}$, $\mathbf{D}_{xy}$, $\mathbf{D}_{yx}$, $\mathbf{D}_{yy}$, $\mathbf{B}_x$, $\mathbf{B}_y$, $\mathbf{C}_x$, $\mathbf{C}_y$, and $\mathbf{E}$ as

$$\mathbf{L} = \begin{bmatrix} \mathbf{D}_{xx} & \mathbf{D}_{yx} & Ra\,\mathbf{B}_x \\ \mathbf{D}_{xy} & \mathbf{D}_{yy} & Ra\,\mathbf{B}_y \\ \frac{Bi}{1+Bi}\mathbf{C}_x & \frac{Bi}{1+Bi}\mathbf{C}_y & \mathbf{E} \end{bmatrix}. \quad (29)$$

The matrices **D** contain the Galerkin projections of the viscous dissipation terms, the matrices **B** represent the projections of the buoyancy force, the matrices **C** represent the projections of the convective term of Eq. (16), and the matrix **E** represents the dissipation term of the energy equation:

$$\mathbf{D}_{\eta\xi} = \left[\left\langle \Delta \mathbf{w}_{ijk}^{(\eta)}, \mathbf{w}_{pqr}^{(\xi)} \right\rangle\right], \tag{30}$$

$$\mathbf{B}_{\eta} = \left[\left\langle q_{ijk}, \mathbf{w}_{pqr}^{(\eta)} \cdot \mathbf{e}_z \right\rangle\right], \tag{31}$$

$$\mathbf{C}_{\eta} = \left[\left\langle \mathbf{w}_{ijk}^{(\eta)} \cdot \mathbf{e}_z, q_{pqr} \right\rangle\right], \tag{32}$$

$$\mathbf{E} = [\langle \Delta q_{ijk}, q_{pqr} \rangle], \tag{33}$$

Here η and ζ are x or y, and the pairs of indices (i, p), (j, q), and (k, r) vary from 0 to N_x, N_y, and N_z, respectively, the angular brackets represent the inner product and the square brackets represent assembling all the terms in one matrix. Note that the matrix **L** can be symmetrized if one multiplies Eq. (14) by $Bi/(1+Bi)$ and Eq. (16) by Ra before the Galerkin process starts. This will lead to the multiplication of the first two rows of (29) by $Bi/(1+Bi)$, and the third row by Ra. It is easy to see that such a transformation will not alter the eigenvalues. The eigenvector will change so that components of **X** corresponding to $c_{ijk}^{(x)}$ and $c_{ijk}^{(y)}$ will be multiplied by $Bi/(1+Bi)$, and the components corresponding to d_{ijk} will be multiplied by Ra. Therefore, the patterns of the dominant perturbation modes (which are defined within multiplication by a constant) will not be altered.

The symmetric form of the matrix **L** emphasizes the fact that all the eigenvalues are real numbers and permits us to use effective eigenvalue solvers for symmetric matrices. However, such solvers will be hardly useful for the general case, when the stability of a basic state with non-zero velocity is considered. The code used in the present study is based mainly on the QR decomposition algorithm for the general eigenproblem, which is used in cases when the stability of steady flows with non-zero initial velocity is considered [4–8].

An approximation of the velocity field (22) may be represented also by the vector potential $\mathbf{\Psi} = (\Psi_x, \Psi_y, \Psi_z)$, $\mathbf{v} = rot\mathbf{\Psi}$. Using Eqs. (21)–(24) it can be easily found that $\Psi_{\mathbf{z}} = 0$, and the two other components can be represented as

$$\Psi_x = \sum_{i=0}^{N_x}\sum_{j=0}^{N_y}\sum_{k=0}^{N_z} c_{ijk}^{(x)}(t)\psi_{ijk}^{(x)}(x,y,z), \qquad \Psi_y = \sum_{i=0}^{N_x}\sum_{j=0}^{N_y}\sum_{k=0}^{N_z} c_{ijk}^{(y)}(t)\psi_{ijk}^{(y)}(x,y,z) \tag{34}$$

$$\psi_{ijk}^{(x)} = \sum_{m=0}^{4} \tilde{f}_{im} T_{i+m}\left(\frac{x}{A_x}\right) \sum_{l=0}^{4} \frac{\tilde{g}_{jl}}{2(j+l)} T_{j+l}\left(\frac{y}{A_y}\right) \sum_{n=0}^{4} \frac{\tilde{h}_{kn}}{2(k+n)} T_{k+n}(z) \tag{35}$$

$$\psi_{ijk}^{(y)} = -\sum_{m=0}^{4} \frac{\hat{f}_{im}}{2(i+m)} T_{i+m}\left(\frac{x}{A_x}\right) \sum_{l=0}^{4} \hat{g}_{jl} T_{j+l}\left(\frac{y}{A_y}\right) \sum_{n=0}^{4} \frac{\hat{h}_{kn}}{2(k+n)} T_{k+n}(z). \tag{36}$$

The two scalar functions Ψ_x and Ψ_y can be used to represent the three-dimensional velocity field instead of three components of velocity (see Section 6). In the case of two-dimensional flow in the xz-plane the two-dimensional stream function is represented by Ψ_y, with the dependence on y omitted.

4. VALIDATION OF THE CODE

4.1. *An Infinite Fluid Layer*

The first test case used for the validation of the code was the classical Rayleigh–Bénard problem for stability of the quiescent state of an infinite fluid layer heated from below. Three cases of the boundary conditions were considered: (1) stress-free isothermal horizontal boundaries, (2) no-slip isothermal horizontal boundaries, and (3) stress-free thermally insulated upper and no-slip isothermal lower boundary. Cases (1) and (2) are classical [11, 12] and the critical Rayleigh numbers are $Ra_{cr}^{(1)} = 27\pi^4/4 \approx 657.511$ and $Ra_{cr}^{(1)} \approx 1707.762$, respectively. In the third case, considered in [20], it is assumed that the initial distribution of the temperature is $\theta = 1 - z$ (isothermal boundaries), but the boundary conditions for the perturbation of the temperature are described by (17), (18) with $Bi = 0$. This yields $Ra_{cr}^{(3)} \approx 669$. The last case was used to validate the code for different boundary conditions at the horizontal boundaries.

It is known that the onset of convection in all three problems is caused by two-dimensional perturbations [11, 12]. This allows us to consider rectangular cavities with periodic boundary conditions on the vertical boundaries. The aspect ratio of the cavities was taken equal to half of the critical wavelength. The results for different numbers of the basis functions are summarized in Table I. It is seen that for all three cases the use of 6×6 basis functions provides 3–4 correct digits of Ra_{cr}, and that convergence up to 9–10 digits is reached with the use of 10×10 basis functions. Such a rapid convergence can be explained by the form of the most critical modes, which are sine and cosine in both directions. The Chebyshev polynomials (25) used in the definitions of the basis functions also are forms of sine and cosine and hence provide a very rapid approximation of the latter.

4.2. *Two-Dimensional Cavities*

Convergence of the critical Rayleigh number for two-dimensional cavities is shown in Table II. For $Bi = 1$ (Problem 1) cavities with $A = 1$, 5, and 10 were considered. To ensure convergence for other Bi (Problem 2) the most difficult case with $A = 10$ and $Bi = 10$ was also taken into consideration. The number of basis functions $N_x \times N_z$ was always chosen such that $N_x = (\text{number of rolls}) \times N_z$. The number of convective rolls in the most critical perturbation mode increases with the growth of the aspect ratio (see Section 5). Therefore better resolution in the horizontal direction is needed to resolve the perturbation mode correctly. The results show (see Table II) that four correct digits of Ra_{cr} can be obtained

TABLE I

Critical Rayleigh Number for Onset of Convection in an Infinite Horizontal Fluid Layer

$N_x \times N_z$	Infinite layer with sress-free isothermal boundaries, $Ra_{cr}^{(1)}$	Infinite layer with no-slip isothermal boundaries, $Ra_{cr}^{(2)}$	Infinite layer with boundary conditions (17), (18) for $Bi = 0$, $Ra_{cr}^{(3)}$
2×2	664.86942	1751.19773	683.75248
4×4	657.51854	1708.55024	669.06955
6×6	657.51139	1707.76205	669.03345
8×8	657.51140	1707.76181	669.03345
10×10	657.51140	1707.76181	669.03345

TABLE II
Convergence Study for Finite 2D Cavities with Boundary Conditions (17)–(19)

$A=1$, $Bi=1$ (1 roll)		$A=5$, $Bi=1$ (4 rolls)		$A=10$, $Bi=1$ (7 rolls)		$A=10$, $Bi=10$ (8 rolls)	
$N_x \times N_z$	Ra_{cr}	$N_x \times N_z$	Ra_{cr}	$N_x \times N_z$	Ra_{cr}	$N_x \times N_z$	Ra_{cr}
4×4	3147.8841	8×2	1699.4276	14×2	1602.4762	16×2	1128.7519
6×6	3147.2828	16×4	1648.9375	28×4	1566.0572	32×4	1105.5130
8×8	3147.2654	24×6	1648.8235	42×6	1565.9507	48×6	1105.3999
10×10	3147.2641	32×8	1648.8233	56×8	1565.9506	64×8	1105.3999
12×12	3147.2640	40×10	1648.8233	70×10	1565.9506	80×10	1105.3999
14×14	3147.2640	48×12	1648.8233	84×12	1565.9506	96×12	1105.3999

with $N_x = 6$. Eight digits of Ra_{cr} remain unchanged with the use of $N_x \geq 12$. This ensures the convergence of the numerical method.

Further validation of the numerical method requires comparison with independent numerical data. To validate the coefficients in (23), (24), and (27), defining the boundary conditions, it is necessary to compare with independent results obtained for the considered boundary conditions (17)–(20). To the best of our knowledge, such data was not published yet. Therefore, the necessary comparison is carried out in two separate ways, as follows. First, we compare with the results of [14], obtained for cavities with four no-slip walls. Second, using the unsteady finite volume solver, we produce some independent data for the considered boundary conditions and use it for comparison. The comparison with results of [14] is shown in Table III. The results coincide up to the fourth digit, which provide an additional justification of the described spectral approach. According to our convergence studies (Table II), we can expect more than 4 correct digits in our results reported in Table III.

To validate the converged values of Ra_{cr}, obtained for the considered boundary conditions (17)–(20), a direct straightforward solution of the problem (1)–(7) was carried out using the finite volume method. The method is second order in space and time and was already used for similar purposes in [5–8]. To define the departure from the pure conduction regime (8) we define the Nusselt number as

$$Nu = -\frac{1+Bi}{BiA}\int_0^A \frac{\partial\theta}{\partial z}\,dx. \tag{37}$$

Obviously, $Nu = 1$ corresponds to pure conduction and $Nu > 1$ indicates the presence of convective motion. The relations $Nu(Ra)$ were calculated for the cases $A = 1$, $Bi = 1$ and

TABLE III
Comparison with Results of [14]: Finite 2D Cavities with 4 No-Slip Walls

A	$N_x \times N_z$	Present results	Results of [4]
1	10×10	2585.02	2585.03
2	20×10	2013.21	2013.24
3	30×10	1870.58	1870.72
4	40×10	1810.27	1810.48
5	50×10	1778.56	1779.00

TABLE IV
Elapsed CPU Time (s) for Different Eigensolvers

Parameters	$N_x \times N_z$	1	2	3	4
$A=1$, $Bi=1$	10×10	3.2	2.0	1.6	0.64
$A=5$, $Bi=1$	40×10	330	230	205	35
$A=10$, $Bi=10$	80×10	3320	2020	1890	210

Note. Calculations on workstation DEC 3000. 1, QR eigensolver with non-symmetric matrix; 2, QR eigensolver with symmetrized matrix; 3, QL/QR eigensolver for symmetric matrices; 4, inverse iteration algorithm.

$A=10$, $Bi=10$, using 50×50 and 100×30 uniform grids, respectively. In the first case the onset of convection was found to take place in the interval $3140 < Ra < 3150$, and in the second case $1100 < Ra < 1107$. Both results are in complete agreement with the results of linear stability analysis (Table II).

It should be noticed that the straightforward time-dependent calculations near the critical points are more difficult than far from them. Consider, for example, the case $A=10, Bi=10$. The calculations were done using a 100×30 uniform grid and a time step $\Delta t = 0.01$. Steady state was assumed to be reached when the relative difference between two successive states in each node of the grid was less than $\varepsilon = 10^{-5}$. Calculation for $Ra=1400$, using steady state at $Ra=1500$ as initial guess ($\Delta Ra = 100$), required 920 time steps. A similar calculation for $Ra=1120$, using steady state at $Ra=1130$ as initial guess ($\Delta Ra = 10$), required 1300 time steps. The necessary integration time increases when the Rayleigh number approaches its critical value. This simple example emphasizes the superiority of a direct stability analysis as compared with a straightforward unsteady simulation when hydrodynamic stability problems are considered.

Some characteristic elapsed CPU times needed for the solution of the eigenvalue problem (28) are shown in Table IV. The first case (QR algorithm for the non-symmetric matrix $\mathbf{L}$) is characteristic of the general case with non-zero initial velocity field. The DGEEV driver routine of the LAPACK library was used for this purpose. The necessary CPU time grows approximately as N^3, where N is the total number of degrees of freedom ($N = 2 \times N_x \times N_y$ for 2D convective flows and $N = 3 \times N_x \times N_y \times N_z$ for 3D convective flows). Use of the QR algorithm with the symmetrized matrix (case 2 in Table IV) allows one to reduce the necessary CPU by approximately 30%. The reason for this is the triangular form of the resulting Hessenberg matrix, such that no additional computations are needed to obtain the eigenvalues. A switch from general to symmetric QL/QR eigensolver (DSYEV driver routine of the LAPACK library, case 3 in Table IV) provides an additional speedup of 5–10%. Finally, we tried to use the inverse iteration algorithm to calculate the dominant eigenvalue only. For the first initial guess it was assumed that the dominant eigenvalue is a small positive number, say $\Lambda = 0.1$. In the case when the computation converges to a correct eigenvalue the inverse iteration algorithm (case 4) is faster than previous algorithms (see Table IV). However, it converges only when the dominant eigenvalue is far enough from the rest of the spectrum. Unfortunately this is not the case for the considered problem (see below), as well as for other hydrodynamic stability problems. In cases when several eigenvalues are close (in the considered case—close to zero), the inverse iteration algorithm does not converge, or converges to a wrong result (non-dominant eigenvalue). The reported stability diagrams were obtained with the use of the QR algorithm with the symmetrized matrix $\mathbf{L}$.

TABLE V
Test Calculations for Finite 3D Cavities, $Bi = 1$

$A_x = A_y = 1$		$A_x = A_y = 4$		$A_x = A_y = 8$	
$N_x \times N_y \times N_z$	Ra_{cr}	$N_x \times N_y \times N_z$	Ra_{cr}	$N_x \times N_y \times N_z$	Ra_{cr}
$4 \times 4 \times 4$	4350.3	$6 \times 6 \times 4$	1687.1	$8 \times 8 \times 4$	1590.8
$6 \times 6 \times 6$	4347.2	$8 \times 8 \times 6$	1683.9	$10 \times 10 \times 6$	1579.0
$8 \times 8 \times 8$	4347.1	$10 \times 10 \times 8$	1683.8	$12 \times 12 \times 8$	1577.2
$10 \times 10 \times 10$	4347.1	$12 \times 12 \times 10$	1683.8	$14 \times 14 \times 10$	1577.2

4.3. *Three-Dimensional Cavities*

The three-dimensional part of the code was validated using the results of [21] obtained for a rectangular cavity with no-slip boundaries. Our results for $A = A_x = A_y = 2$ and 6 are $Ra_{cr} = 2085$ and 1755, respectively. The corresponding results of [21] are $Ra_{cr} = 2107$ and 1765. Several examples of convergence study for cavities with $A_x = A_y = A$ (Problem 4) are shown in Table V. Compared to the two-dimensional case the total number of degrees of freedom increases by a factor of $1.5 \times N_y$. Therefore it was not possible to perform the convergence study with as much detail as it was done for 2D cavities. However, the results reported in Table V together with the conclusions made in the preceding subsection allow us to be quite confident in 4–5 correct digits of Ra_{cr} when using $10 \times 10 \times 8$ basic functions for $A \le 4$, and $12 \times 12 \times 8$ basic functions for $A \le 8$. It is seen (Table V) that results obtained for small number of the basis functions (with poor spatial resolution) overestimate values of Ra_{cr}. The above small discrepancy between our results and results of [21] can be explained by fewer number of Galerkin modes used for the calculations [21]. Besides this, during the EUROMECH Colloquium 383, we compared our critical values with results of other authors (not published yet). Comparisons made mainly for $A = A_x = A_y = 1$ and 3 showed good agreement between different numerical approaches used.

The characteristic CPU times for the corresponding eigenproblems are (QR decomposition algorithm for symmetrized matrix $\mathbf{L}$) 2600 s for $8 \times 8 \times 8$ basis functions (1536 degrees of freedom) on DEC 3000 workstation; 3500 s for $12 \times 12 \times 8$ functions (3456 degrees of freedom) on CRAY J90 with 8 processors.

5. RESULTS FOR THE TWO-DIMENSIONAL CASE

The marginal stability curve $Ra_{cr}(A)$ for $Bi = 1$ is plotted in Fig. 1. It consists of several continuous parts, which correspond to the different most critical modes. In cases of instabilities due to Hopf bifurcation, different most critical perturbation modes can be distinguished by abrupt changes of the critical frequencies of oscillations [5–8]. In the present case, however, the only way to distinguish between the different perturbation modes is to plot the corresponding patterns of the most critical perturbations. Clearly, at the points where one critical mode is replaced by another one the critical Rayleigh numbers of both modes are close. Therefore, it is not enough to compare only the calculated values of Ra_{cr}, because close values can belong to different perturbation modes. Patterns of the dominant perturbations also must be compared. For that reason we have to extend the Problem 3 and to plot *the different patterns* of the most critical modes. These different modes differ by the number of convective rolls and are included in Fig. 1 as insets. Furthermore, to make a complete comparison between different numerical approaches it is necessary to compare the values of the

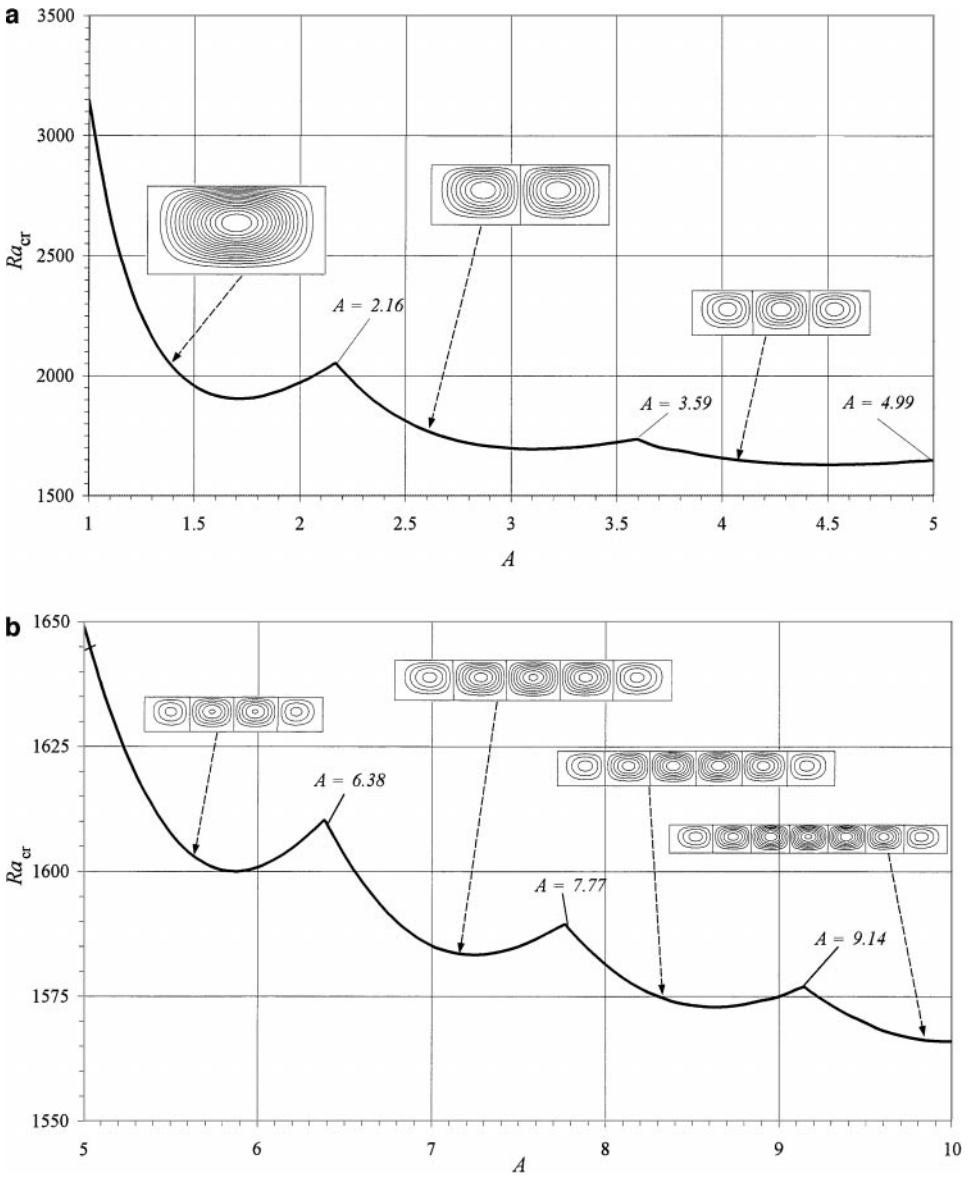

FIG. 1. Dependence of the critical Rayleigh number on the aspect ratio. Two-dimensional case. $Bi = 1$. (a) $1 \le A \le 5$, (b) $5 \le A \le 10$.

aspect ratio where one dominant mode is replaced by another one. These values are shown in Fig. 1, as well as in all stability diagrams corresponding to other 2D and 3D cases. It should be mentioned that the increase of the number of two-dimensional Rayleigh–Bénard convective rolls with the increase of the aspect ratio is well known [13–15].

The dependence $Ra_{cr}(Bi)$ for $A = 10$ is shown in Fig. 2. In this case only one change of the most critical perturbation mode (from seven to eight convective rolls) was found at $Bi = 2.34$. Patterns of the corresponding most critical modes are shown as insets in Fig. 2.

It should be noted also that at large supercriticalities, where several perturbation modes are unstable, one can expect the existence of multiple steady (and probably also oscillatory)

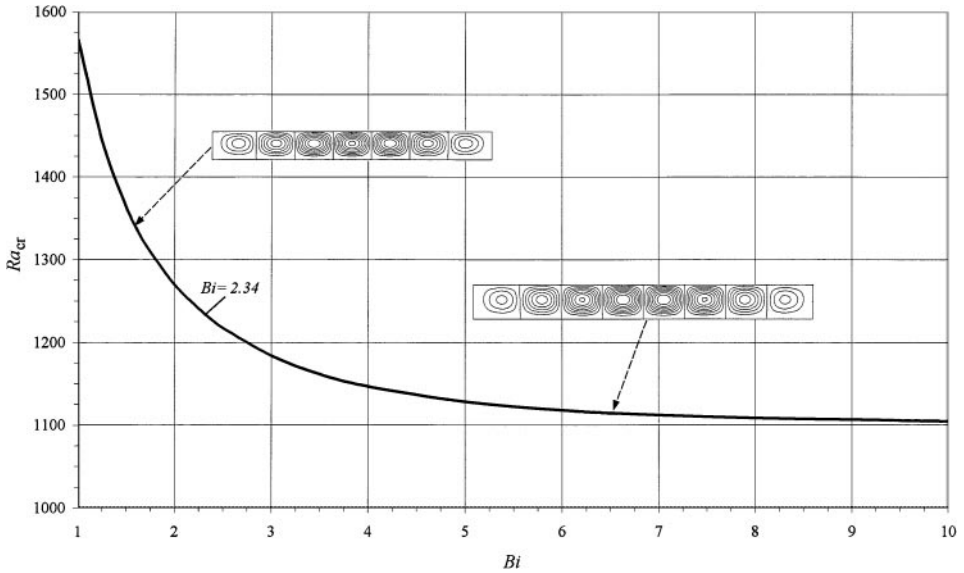

FIG. 2. Dependence of the critical Rayleigh number on the Biot number. Two-dimensional case. $A = 10$.

states of the convective flow. The resulting asymptotic state will depend not only on the governing parameters but also on the initial state of the flow.

6. RESULTS FOR THE THREE-DIMENSIONAL CASE

6.1. *Problem 4: Square Horizontal Cross Section,* $1 \le A = A_x = A_y \le 8$

The neutral curve for Problem 4 ($1 \le A = A_x = A_y \le 8$) is shown in Fig. 3. Similarly to the two-dimensional case, there are several modes of the most dangerous perturbation which replace each other when A is varied. However, the spectrum of possible perturbations is more complicated in the three-dimensional case. The larger variety of perturbations is obviously caused by the three-dimensional geometry. An additional complexity is caused by the variety of the symmetries of the problem (see below). Values of critical Rayleigh numbers corresponding to different perturbation modes are close which makes it difficult to indicate the most dangerous one. The last statement is illustrated in Table VI which lists the largest eigenvalues in the interval $[-1, 0]$, calculated for the case $A = 1.7$, at the critical Rayleigh number $Ra_{cr} = 2355.2$. Note that at $Ra = 2400$ the dominant eigenvalue is already larger than 20, $\lambda_{\max} = 29.91$. In the considered case (Table VI) there are 4 multiple and 7 simple eigenvalues which are relatively close to zero. It is obvious that at larger Ra more modes become unstable which can lead to an appearance of multiple steady states. Recently, seven different supercritical steady states in a cubic cavity heated from below were calculated in [22].

Following [18] we denote symmetry classes *EE*, *EO*, *OE*, and *OO* for functions which are *e*ven or *o*dd with respect to the midplanes $x = A_x/2$ and $y = A_y/2$, respectively. Furthermore, we denote symmetry classes *RS* and *RA* for functions which are *s*ymmetric and *a*ntisymmetric, respectively, with respect to 180° *r*otation around the vertical axis that passes through the center of the horizontal cross section (line $x = A_x/2$, $y = A_y/2$). Note that the *EE* class is a subset of the *RS* class (the *OO* class is a subset of the *RA* class); however,

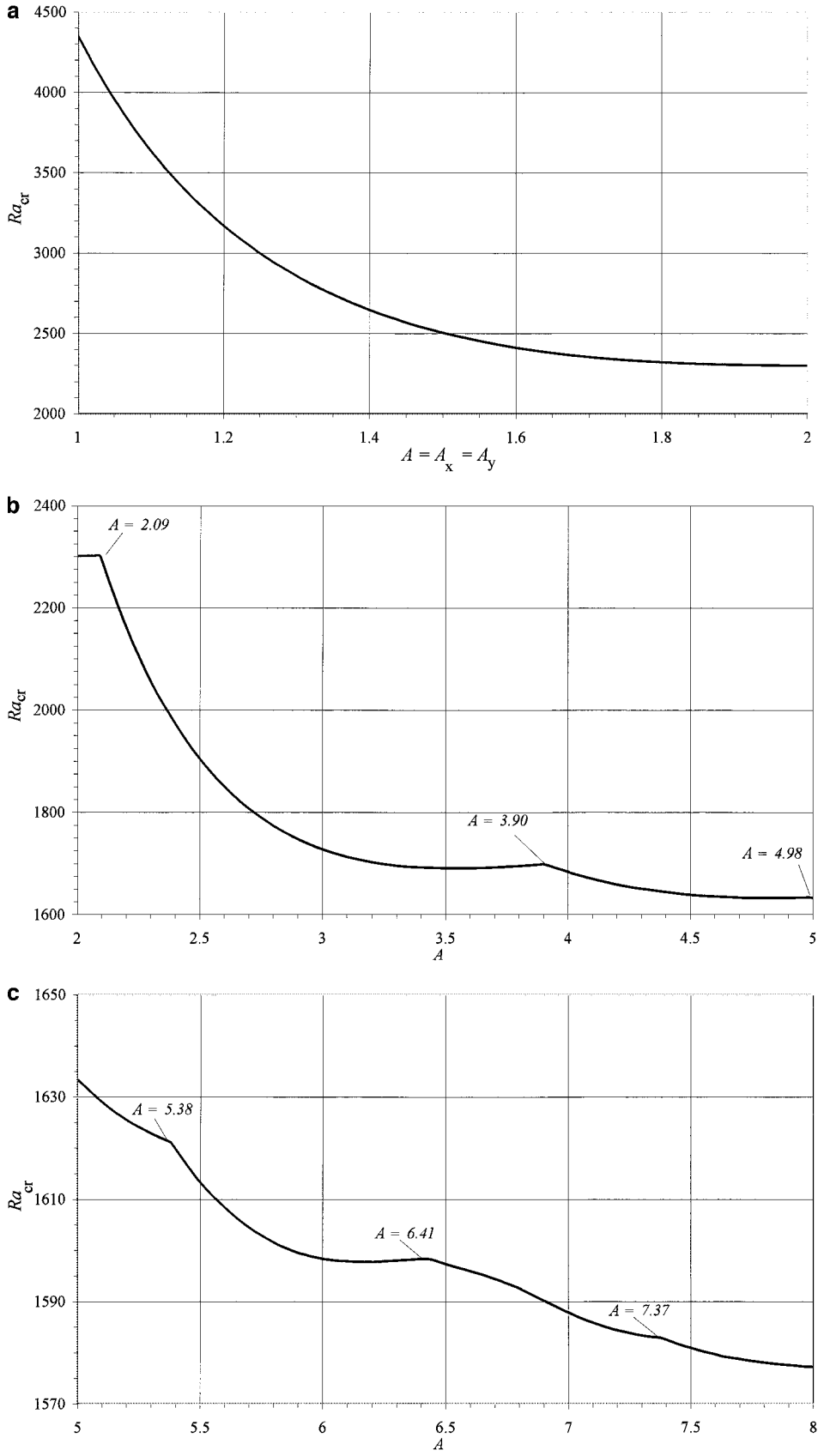

FIG. 3. Dependence of the critical Rayleigh number on the aspect ratio $A = A_x = A_y$. Three-dimensional case. $Bi = 1$. (a) $1 \le A \le 2$, (b) $2 \le A \le 5$, (c) $5 \le A \le 8$.

TABLE VI
Larget Eigenvalues $0 \leq \lambda \leq 1$ Found for *Ra* = 2355.2 and *A* = 1.7

No.	λ	Multiplicity
1	0	2
2	−0.3276	1
3	−0.3402	2
4	−0.3717	1
5	−0.5585	1
6	−0.5681	2
7	−0.5694	1
8	−0.6196	1
9	−0.6536	2
10	−0.7230	1
11	−0.9608	1
12	−0.9991	1

these classes do not coincide (see Figs. 4 and 5, for example). Note also that in cavities with square horizontal cross section the classes *EO* and *OE* are identical, and the classes *RS* and *RA* are defined to within a 90° rotation around the same axis. This leads to a multiplicity of the corresponding eigenvalues. For example, the leading eigenvalue in Table VI corresponds to the perturbation with *RA* symmetry and has a multiplicity of 2. It should be noted also that symmetries of all scalar functions considered (three components of velocity and

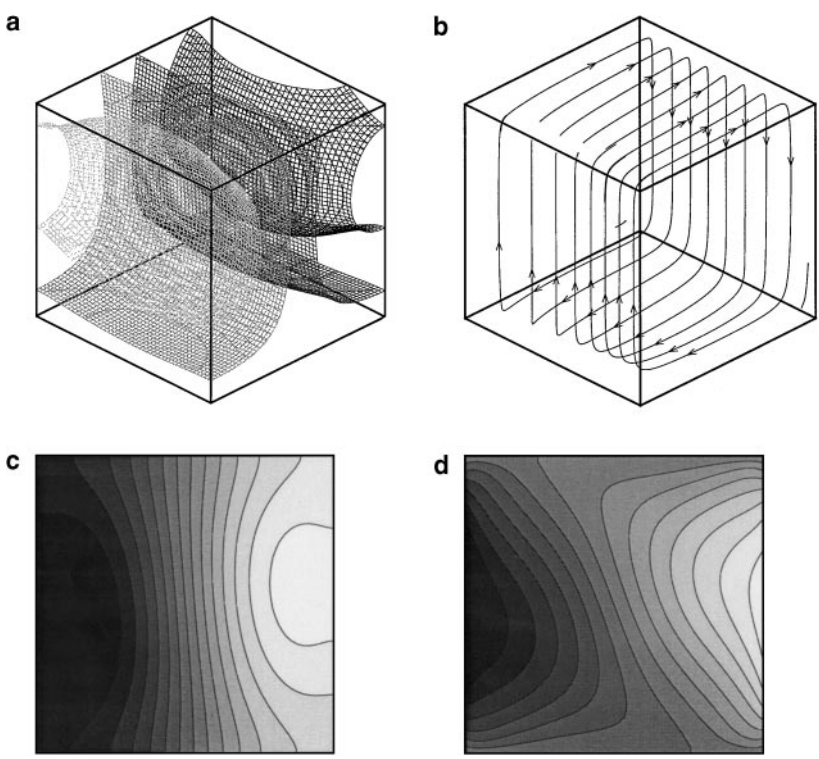

FIG. 4. Perturbation at $A_x = A_y = 1$, $Bi = 1$, $Ra_{cr} = 4347$. (a) Perturbation of temperature, (b) streaklines of perturbation of velocity, (c) isotherms, and (d) vertical velocity contours in the mid-height cross section.

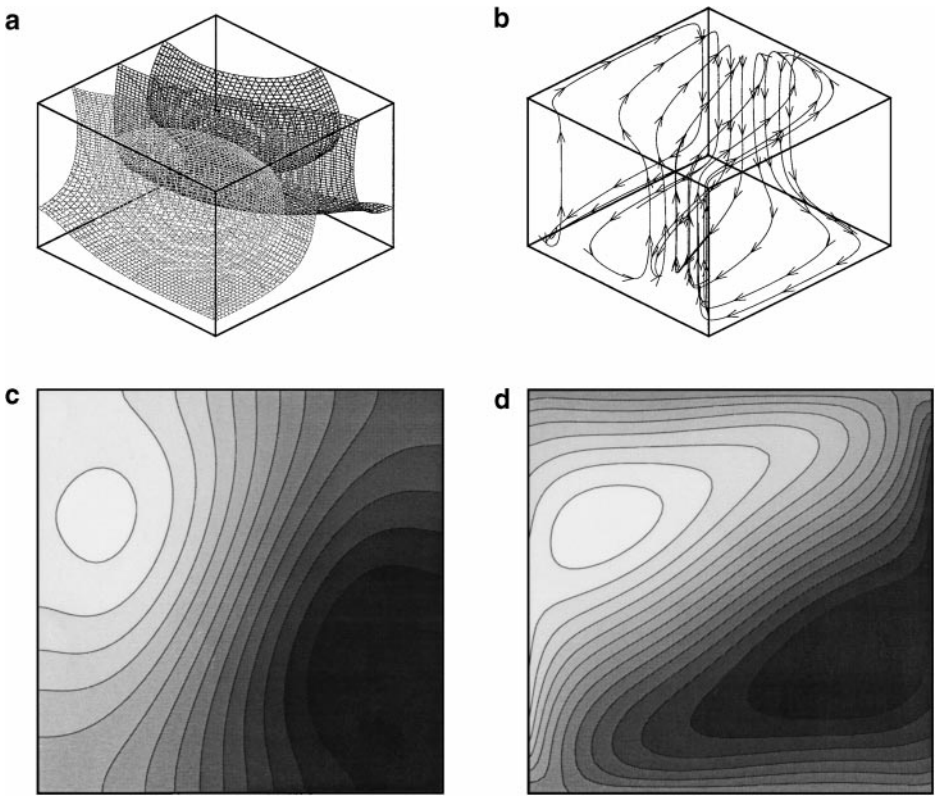

FIG. 5. Perturbation at $A_x = A_y = 1.5$, $Bi = 1$, $Ra_{cr} = 2506$. Same as Fig. 4.

temperature) do not necessarily coincide. Therefore we use only the temperature and the vertical velocity, whose symmetries necessarily coincide (larger temperature causes rising of the fluid), to characterize the symmetry properties of the perturbation patterns.

It follows from the multiplicity of the perturbation modes that comparison of values of the critical Rayleigh number only is not sufficient to ensure that different codes yield similar results. It is necessary also to compare the patterns of the most dangerous perturbation at several characteristic points and to compare the values of A where different perturbation modes replace each other (as we suggested for the two-dimensional case). These values of the aspect ratio are shown in Fig. 3. The characteristic patterns of the most dangerous perturbations of the temperature and velocity are illustrated in Figs. 4–11. To visualize velocity we use streaklines calculated using the calculated perturbation of velocity. Note that in the three-dimensional case the streaklines are not necessarily closed curves. As it follows from the following figures, a liquid particle can travel from one convective roll to another (see also [22]). In the following text the word "perturbation" will be used instead of the term "the most dangerous perturbation."

At $A = A_x = A_y = 1$ (Fig. 4) the perturbation is similar to the one obtained for the two-dimensional case (Fig. 1a) and appears as a roll where hot liquid rises along one vertical wall and cold liquid descends along the opposite wall. The perturbations of temperature and vertical velocity belong to the *RA* symmetry class (Figs. 4c and 4d). At larger values of A this perturbation pattern deforms such that the flow trajectories and temperature isosurfaces tend to turn away from the walls towards the diagonal planes (Fig. 5) and therefore become different from their two-dimensional analogues. However, the *RA* symmetry is preserved

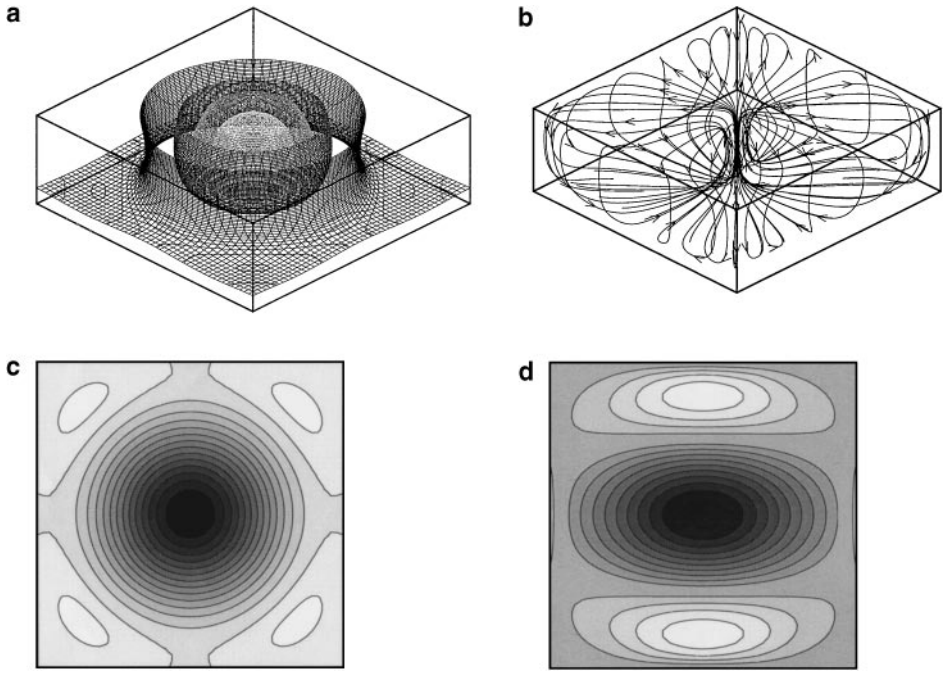

FIG. 6. Perturbation at $A_x = A_y = 3$, $Bi = 1$, $Ra_{cr} = 1728$. Same as Fig. 4.

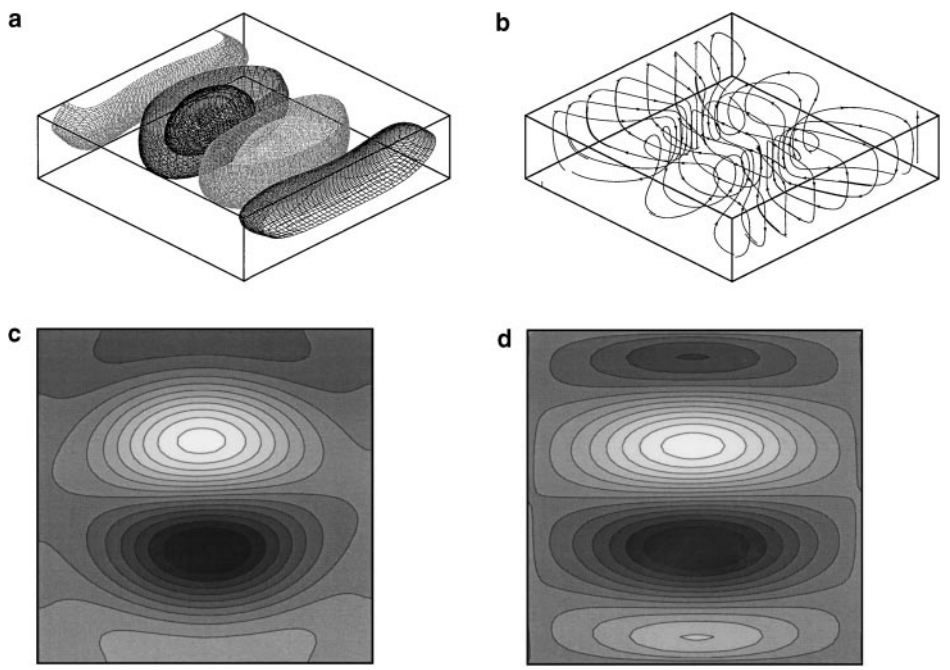

FIG. 7. Perturbation at $A_x = A_y = 4$, $Bi = 1$, $Ra_{cr} = 1684$. Same as Fig. 4.

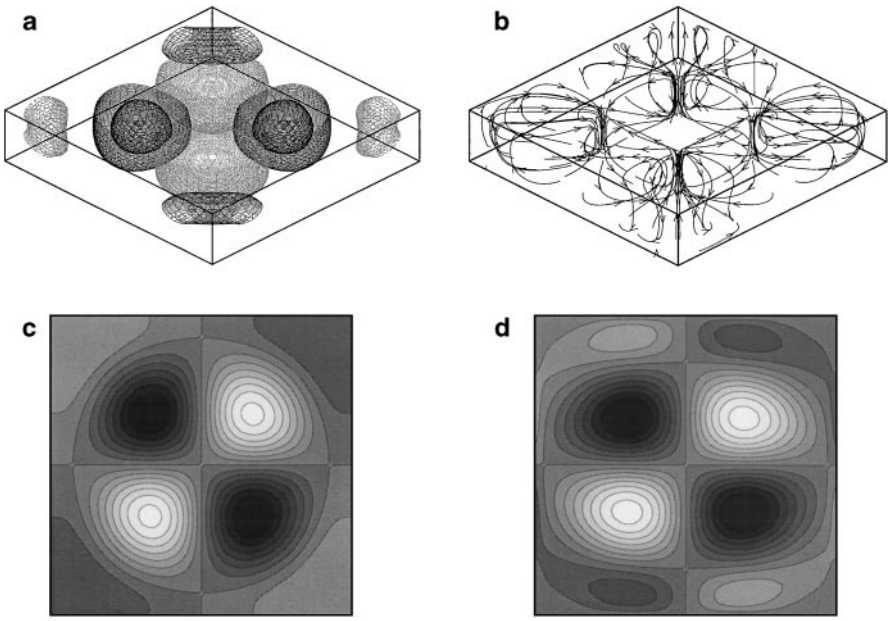

FIG. 8. Perturbation at $A_x = A_y = 5$, $Bi = 1$, $Ra_{cr} = 1633$. Same as Fig. 4.

(Figs. 5c and 5d). At $A = 2.09$ (Fig. 3a) this perturbation is replaced by another one (Fig. 6), where the hot liquid rises at the center of the cavity and the cold liquid descends along the vertical walls. A cross section by a vertical midplane yields the pattern which is similar to a two-dimensional one shown in Fig.1a for the interval including $A = 3$. However, the toroidal shape of the convective roll cannot be predicted on the basis of a two-dimensional calculation. The perturbations of temperature and vertical velocity in this case belong to the *EE* symmetry class (Figs. 6c and 6d).

The next change of perturbation takes place at $A = 3.90$ (Fig. 3b). The corresponding perturbation belongs to the *RA* symmetry class and consists of three convective rolls (Fig. 7).

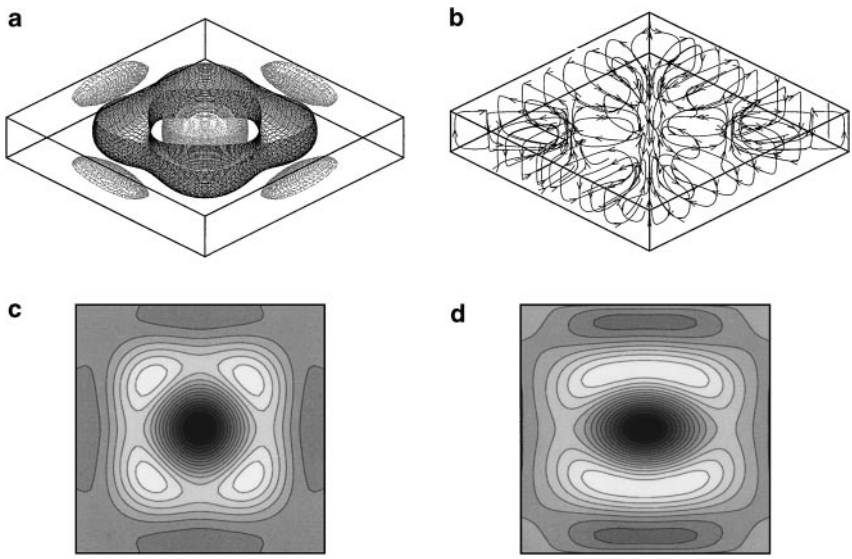

FIG. 9. Perturbation at $A_x = A_y = 6$, $Bi = 1$, $Ra_{cr} = 1598$. Same as Fig. 4.

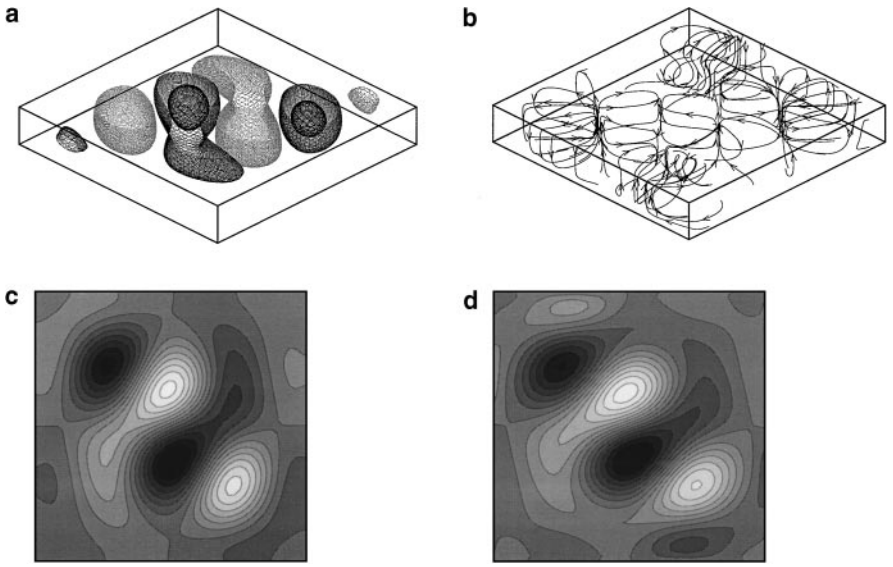

FIG. 10. Perturbation at $A_x = A_y = 6.5$, $Bi = 1$, $Ra_{cr} = 1597$. Same as Fig. 4.

This perturbation pattern in a vertical midplane cross section looks similar to the corresponding two-dimensional result (Fig. 1a). Another perturbation, belonging to the *OO* symmetry class (Fig. 8), appears to be the most dangerous at $A = 4.98$ (Fig. 3b). It consists of four rolls, located in the corners, with the hot fluid rising near two opposite corners and descending near two other corners (Fig. 8b). This perturbation is replaced at $A = 5.38$ by another one which belongs to the *EE* symmetry class (Fig. 9). It consists of two toroidal rolls, one inside another, with the hot fluid descending near the walls and the center (Fig. 9b).

It is more difficult to describe the flow arising as a result of bifurcations corresponding to the two last branches of the neutral curve (Fig. 3c). The perturbation which is the most dangerous in the interval $6.41 < A < 7.37$ is illustrated in Fig. 10. Here one can see strong

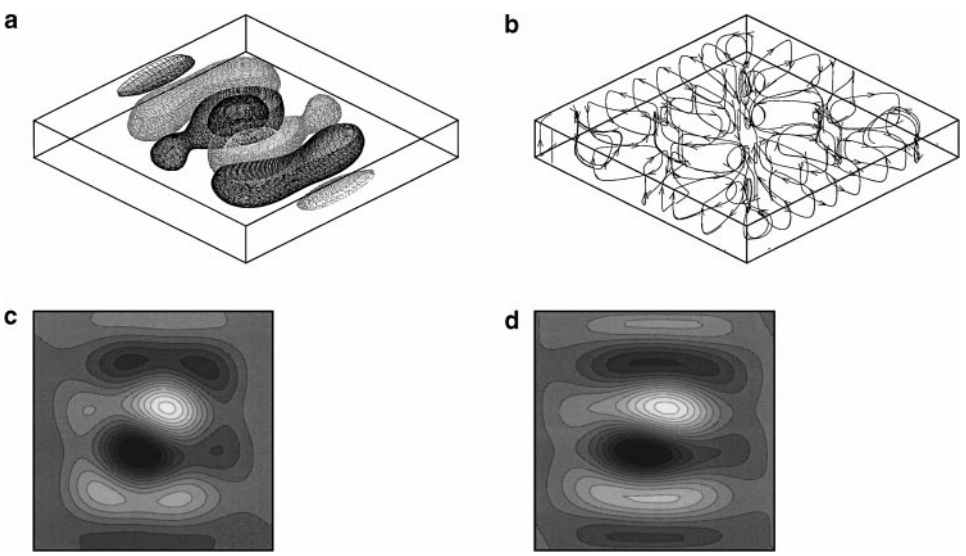

FIG. 11. Perturbation at $A_x = A_y = 7$, $Bi = 1$, $Ra_{cr} = 1588$. Same as Fig. 4.

upflow and downflow in two opposite corners, while in two other corners the convective motion is weaker. The symmetry of the perturbation clearly belongs to the class *RA*.

The last perturbation corresponding to the neutral curve shown in Fig. 3 is illustrated in Fig. 11. This perturbation also belongs to the *RA* class, but now the upflow and the downflow occur near the opposite walls.

6.2. *Problem 5:* $A_x = 4$, $1 \le A_y \le 8$

The neutral curve for this case is shown in Fig. 12. Similarly to the previous case the points where one perturbation is replaced by another one are shown on the graph. Patterns of the most dangerous perturbations are shown in the following figures.

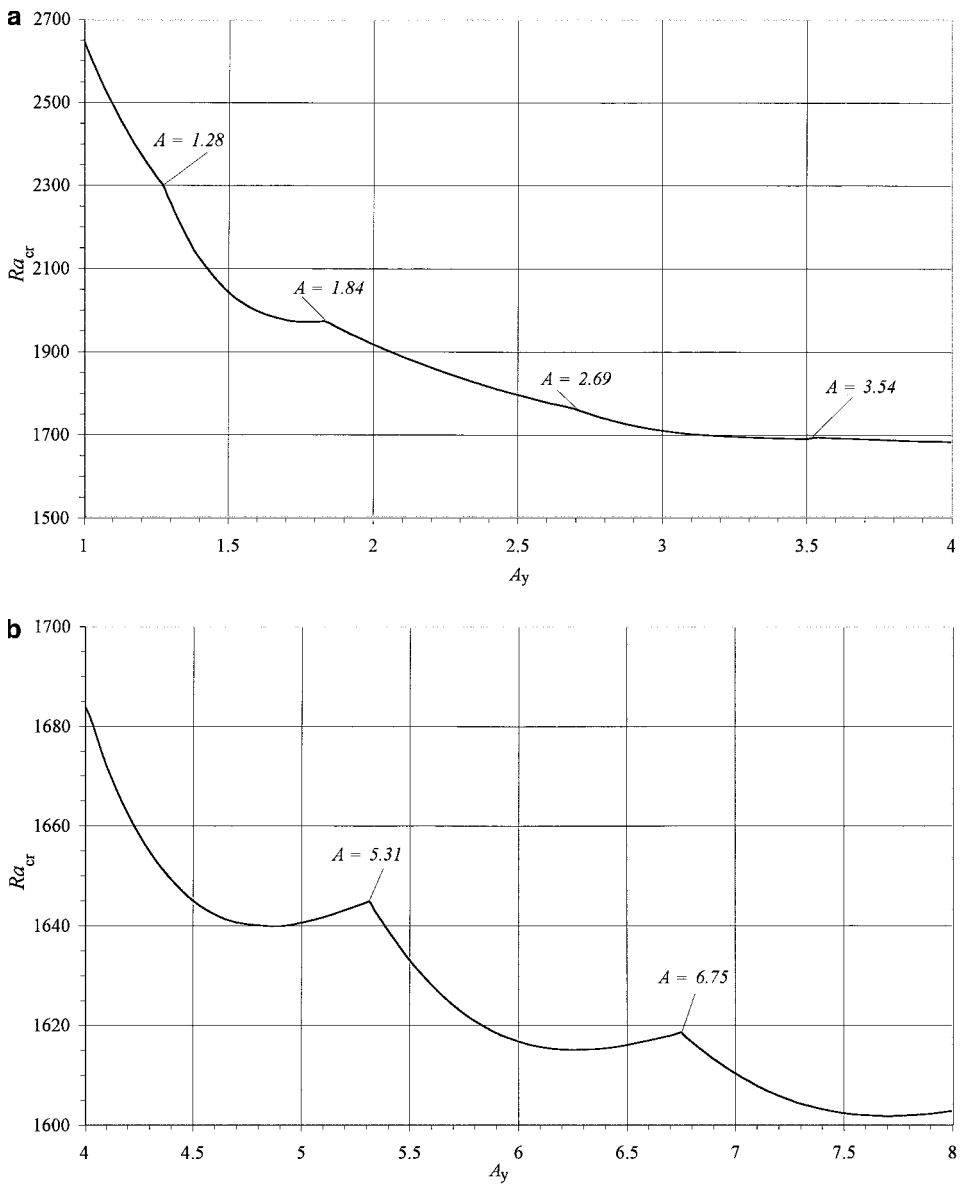

FIG. 12. Dependence of the critical Rayleigh number on the aspect ratio $A_x = 4$, $1 \le A_y \le 8$. Three-dimensional case. $Bi = 1$. (a) $1 \le A_y \le 4$, (b) $4 \le A_y \le 8$.

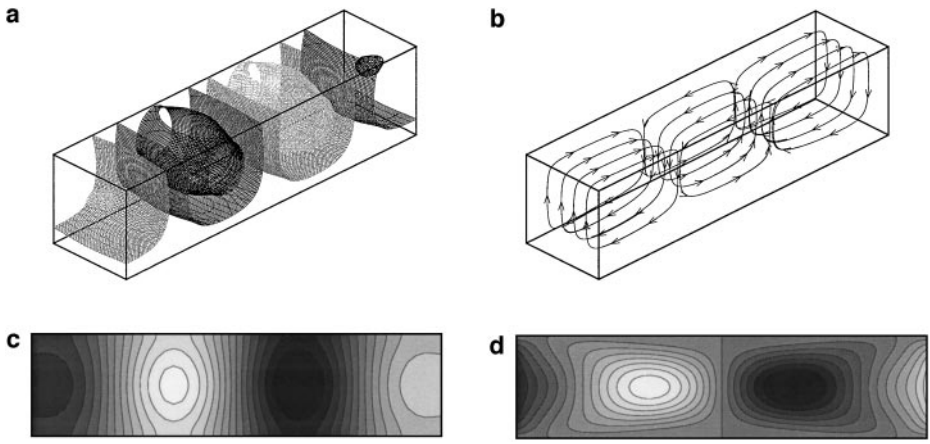

FIG. 13. Perturbation at $A_x = 4$, $A_y = 1$, $Bi = 1$, $Ra_{cr} = 2645$. Same as Fig. 4.

At $A_y = 1$ (Fig. 13) the perturbation belongs to the *OE* symmetry class and consists of three convective rolls parallel to the shorter lateral boundary. In the cross section $y = 0.5$ it looks similar to the two-dimensional perturbation at $A^{2D} = 4$ (Fig. 5a, A^{2D} denotes the two-dimensional aspect ratio). At $A_y = 1.28$ (Fig. 12a) it is replaced by the *EO*-symmetric perturbation which consists of a single roll situated along the longer lateral boundary (Fig. 14). A similarity with the two-dimensional case also can be found, but in this case one has to compare the cross section $x = 2$ with the 2D perturbation at $A^{2D} = 1$. The next change of the perturbation takes place at $A_y = 1.84$. The next perturbation is *OE*-symmetric and consists of three rolls situated along the longer lateral boundary (Fig. 15). Again, the cross section $x = 2$ shows similarity with the two-roll 2D perturbation characteristic for $A^{2D} > 3.59$ (not $A^{2D} = 2$, see Fig. 1a). Note that in spite of the clear similarity between the 3D and 2D perturbations it is impossible to foresee in which cross section of the three-dimensional container the similarity will exist.

The perturbations which become the most dangerous at $A_y = 2.59$ and $A_y = 3.54$ (Fig. 12a) have patterns similar to those reported in Figs. 6 and 7 for $A = A_x = A_y = 3$

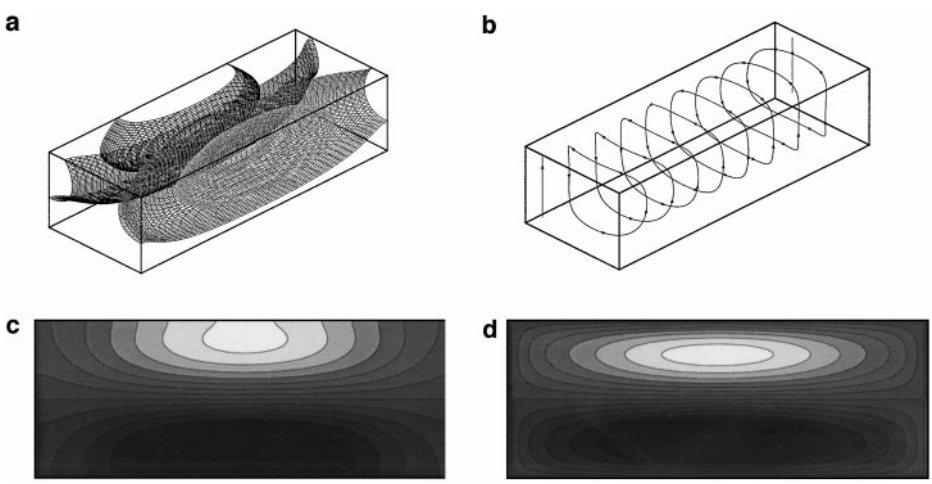

FIG. 14. Perturbation at $A_x = 4$, $A_y = 1.5$, $Bi = 1$, $Ra_{cr} = 2043$. Same as Fig. 4.

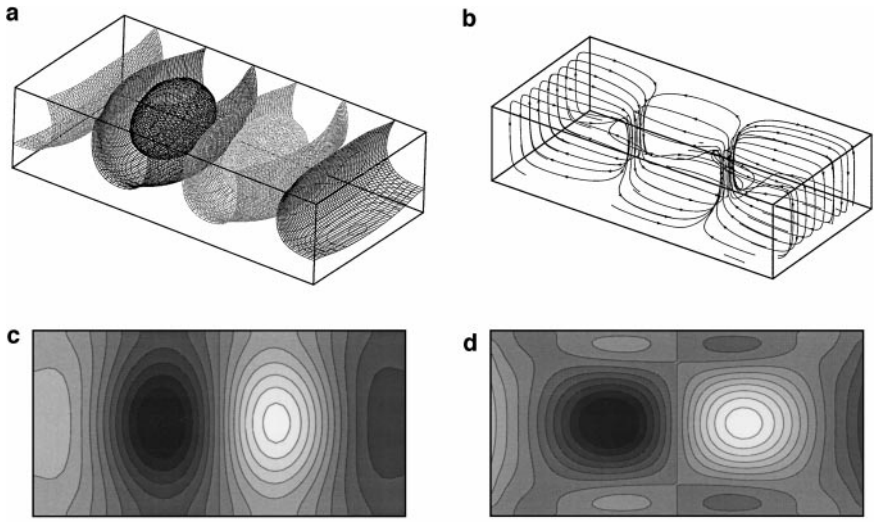

FIG. 15. Perturbation at $A_x = 4$, $A_y = 2$, $Bi = 1$, $Ra_{cr} = 1918$. Same as Fig. 4.

and $A = A_x = A_y = 4$, respectively. The two perturbations characteristic for the two last branches of the neutral curve are illustrated in Figs. 16 and 17. The perturbation which is most dangerous for $5.31 \leq A_y \leq 6.75$ (Fig. 16) is *EE*-symmetric and has two main convective rolls located near the shorter lateral boundaries. Convective motion outside the main rolls is weak and has no definite roll structure. This perturbation has no two-dimensional analog. The next perturbation, most dangerous for $A_y \geq 6.75$ (Fig. 17), is *OE*-symmetric and consists of 5 transverse rolls directed along the shorter lateral boundaries. This perturbation is similar to the two-dimensional one (see the perturbation shown in Fig. 1b for $A^{2D} = 7$).

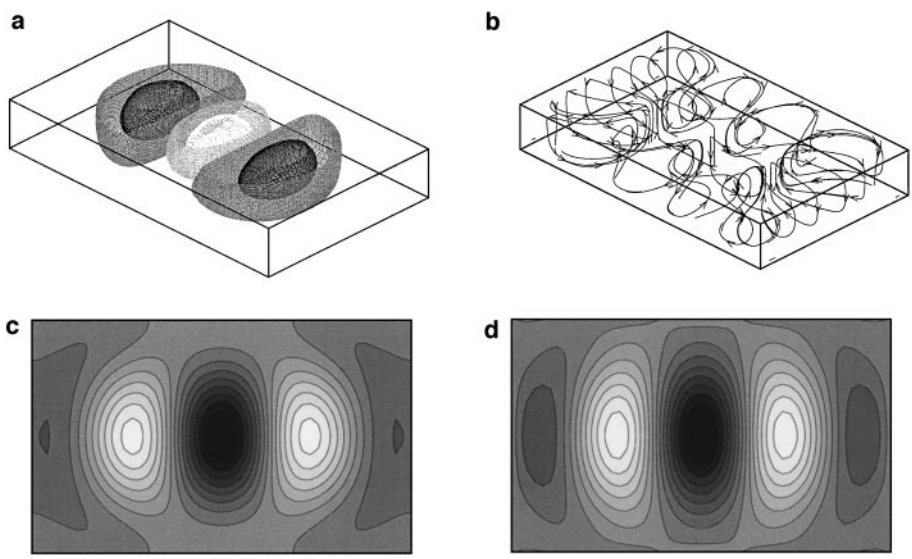

FIG. 16. Perturbation at $A_x = 4$, $A_y = 6.5$, $Bi = 1$, $Ra_{cr} = 1617$. Same as Fig. 4.

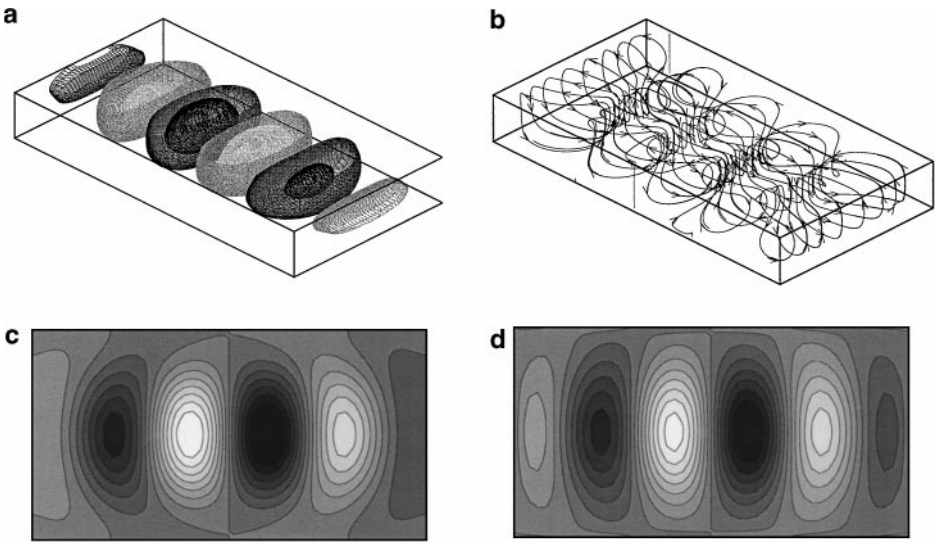

FIG. 17. Perturbation at $A_x = 4$, $A_y = 7.5$, $Bi = 1$, $Ra_{cr} = 1603$. Same as Fig. 4.

CONCLUSIONS

The problem considered here deals with the spectrum of linear terms of the Navier–Stokes and energy equations in the Boussinesq approximation. This problem does not require very good spatial resolution and therefore can be treated with relative ease numerically. Obviously, more realistic problems devoted to the *numerical study of the stability of numerically calculated flows* will involve also the calculation of the basic flow. Then it will be necessary to reach a sufficient accuracy for both basic state and the most dangerous perturbation. In the case of boundary layers [5, 6] or multiplicity of the basic states [8] the problem can become extremely difficult. In view of this the considered benchmark can be attractive for those who start the numerical stability analysis and need validation of their numerical schemes and eigensolvers. On the other hand it can be used only as as a preliminary validation and should be completed by solution of a problem with an *a priori* unknown basic state.

The physics of the Rayleigh–Bénard instability is very well understood [11–13]. However, the results obtained here for a particular rectangular geometry lead to an additional conclusion. It was shown that several different perturbations of the basic quiescent state become critical at close values of the Rayleigh number. This means that in a supercritical state any of these perturbations can grow and the final asymptotic state will depend on the initial conditions. Therefore multiple supercritical steady states can be expected here. This fact should be taken into account when experimentally observed or numerically obtained supercritical flows are compared. It was mentioned already that seven distinct branches of supercritical states for the Rayleigh–Bénard convection in a cube were calculated recently in [22]. Multiple patterns of Bénard–Marangoni instability in three-dimensional boxes were also obtained in [18] using a spectral approach similar to one described here.

There exists a certain similarity between the patterns of two- and three-dimensional perturbations. However, without a proper calculation it is impossible to predict for which geometry and in which cross section the patterns are similar.

The problem discussed above was formulated as a "benchmark problem" for the ERCOFTAC/EUROMECH Colloquium 383. As mentioned, our analysis is a complete (and somewhat extended) solution of the problem. Apparently other solutions presented at the Colloquium were less extensive, which precludes a detailed comparison. Hopefully, other complete solutions will become available in future. Comparison of results of the considered benchmark should then be done in the three following stages:

(1) comparison of values of critical Rayleigh numbers and neutral curves;

(2) comparison of values of the aspect ratio where most dangerous perturbations replace each other;

(3) comparison of patterns of the most dangerous perturbations.

ACKNOWLEDGMENTS

The comments of P. Bar-Yoseph and A. Solan are gratefully acknowledged. This work was supported by the Israel Science Foundation under Grant 110/96-1, by the Israel Ministry of Science under Grant 8575-1-98, by the Center for Absorption in Science, Israel Ministry of Immigrant Absorption, and by the Y. Winograd Chair of Fluid Mechanics and Heat Transfer.

REFERENCES

1. H. A. Dijkstra, Test problem: Rayleigh–Bénard convection, http://www.cs.kuleuven.ac.be/kurt/EUROMECH383/testproblem-en.html.
2. W. S. Edwards, L. S. Tuckerman, R. A. Friesner, and D. C. Sorensen, Krylov methods for the incompressible Navier–Stokes equations, *J. Comput. Phys.* **110**, 82 (1994).
3. K. A. Cliffe, T. J. Garratt, and A. Spence, Eigenvalues of the discretized Navier–Stokes equation with application to the detection of Hopf bifurcations, *Adv. Comput. Math.* **1**, 337 (1993).
4. A. Yu. Gelfgat and I. Tanasawa, Numerical analysis of oscillatory instability of buoyancy convection with the Galerkin spectral method, *Numer. Heat Transfer Part A Appl.* **25**(6), 627 (1994).
5. A. Yu. Gelfgat, P. Z. Bar-Yoseph, and A. Solan, Stability of confined swirling flow with and without vortex breakdown, *J. Fluid Mech.* **311**, 1 (1996).
6. A. Yu. Gelfgat, P. Z. Bar-Yoseph, and A. Solan, Vortex breakdown and instability of swirling flow in a cylinder with rotating top and bottom, *Phys. Fluids* **8**(10), 2614 (1996).
7. A. Yu. Gelfgat, P. Z. Bar-Yoseph, and A. L. Yarin, On oscillatory instability of convective flows at low Prandtl number, *J. Fluids Eng.* **119**, 823 (1997).
8. A. Yu. Gelfgat, P. Z. Bar-Yoseph, and A. L. Yarin, Stability of multiple steady states of convection in laterally heated cavities, *J. Fluid Mech.* **388**, 315 (1999).
9. B. Roux (Ed.), Numerical simulation of oscillatory convection in low-Pr fluids: A GAMM workshop, in *Notes on Numerical Fluid Mechanics* (Vieweg, Braunschweig, 1990), Vol. 27.
10. K. H. Winters, A bifurcation analysis of oscillatory convection in liquid metals, Proc. GAMM Workshop on numerical solution of oscillatory convection in Low prandtl number fluids, in *Notes on Numerical Fluid Mechanics*, edited by B. Roux (Vieweg, Braunschweig, 1990), Vol. 27, p. 319.
11. S. Chandrasekhar, *Hydrodynamic and Hydromagnetic Stability* (Clarendon, Oxford, 1961).
12. G. Z. Gershuni and E. M. Zhukhovitskii, *Convective Stability of Incompressible Fluids* (Israel Program for Scientific Translations, Jerusalem, 1976).
13. E. L. Koschmieder, *Bénard Cells and Taylor Vortices* (Cambridge Univ. Press, Cambridge, UK, 1993).
14. J. M. Luijkx, and J. K. Platten, On the onset of free convection in a rectangular channel, *J. Non-Equilibrium Thermodynam.* **6**, 141 (1981).
15. J. Prat, I. Mercader, and E. Knobloch, Resonant mode interactions in Rayleigh–Bénard convection, *Phys. Rev. E* **58**, 3145 (1998).

16. K. H. Winters, Th. Plesser, and K. A. Cliffe, The onset of convection in a finite container due to surface tension and buoyancy, *Phys. D* **29**, 387 (1988).
17. H. A. Dijkstra, M. J. Molemaker, A. van der Ploeg, and F. F. Botta, An efficient code to compute non-parallel steady flows and their linear stability, *Comput. & Fluids* **24**, 415 (1995).
18. G. B. Dauby and G. Lebon, Bénard–Marangoni instability in rigid rectangular containers, *J. Fluid Mech.* **329**, 25 (1996).
19. A. Zebib, A Chebyshev method for the solution of boundary value problems, *J. Comput. Phys.* **53**, 443 (1984).
20. S. H. Davis and G. M. Homsy, Energy stability theory for free-surface problems: Buoyancy-thermocapillary layers, *J. Fluid Mech.* **98**, 527 (1980).
21. D. F. Edwards, Crossed rolls at onset of convection in a rigid box, *J. Fluid Mech.* **191**, 583 (1988).
22. J. Pallares, F. X. Grau, and F. Girlt, Flow transitions in laminar Rayleigh–Bénard convection in a cubical cavity at moderate Rayleigh numbers, *Int. J. Heat Mass Transfer* **43**, 753 (1999).
23. L. Q. Tang and T. T. H. Tsang, Temporal, spatial and thermal features of 3-D Rayleigh–Bénard convection by a least-squares finite element method, *Comput. Methods Appl. Mech. Engrg.* **140**, 201 (1997).